Supporting information for

Fabrication and design of new redox active azure A/3D graphene aerogel and conductive trypan blue–nickel MOF nanosheet array electrodes for an asymmetric supercapattery

Tahereh Sadeghian Renani[1], Seyyed Mehdi Khoshfetrat[2], Jalal Arjomandi[1, 3, *], Hu Shi[3], Sadegh Khazalpour[4]

[1]Department of Physical Chemistry, Faculty of Chemistry, Bu-Ali Sina University, 65178 Hamedan, Iran

[2]Chemistry Department, Faculty of Science, Ayatollah Boroujerdi University, Boroujerd, Iran

[3]School of Chemistry and Chemical Engineering, Shanxi University, Taiyuan, China

[4]Department of Analytical Chemistry, Faculty of Chemistry, Bu-Ali Sina University, 65178 Hamedan, Iran

[*]To whom correspondence should be addressed, E-mail: j_arjomandi@basu.ac.ir, (ORCID.ID: 0000-0002-7287-1927), Tel: +988138288807, Fax: +988138257407

.....

Figure and Table Captions

Fig. S1. UV-vis absorption of (a) pure Az, GO, Az/GO and (b) Try, $Ni_3(Cl)_2(OH)_4$ and Try-Ni-MOF aqueous solutions.

Fig. S2. UV-vis. absorption spectra of (a) pure azure A and Az/GA and (b) pure trypan blue and Try-Ni-MOF in 3.0 M KOH solution using three electrode cell setup after completing 500 galvanostatic charge-discharge cycles, respectively.

Fig. S3. XRD patterns of (a) GO, GA, and Az–GA and (b) Try, $Ni_3Cl_2(OH)_4$, and the Try–Ni-MOF.

Fig. S4. SEM images of GO.

Fig. S5. N2 adsorption/desorption isotherms of the (a) GA and Az-GA, and (b) $Ni_3Cl_2(OH)_4$ and Try-Ni-MOF samples. The insets are BJH pore size distribution curves.

Fig. S6. EDS spectra of the (a) GO, (b) Az-GA and mapping of the AZ-GA sample.

Fig. S7. EDS spectra and mapping of the (a) $Ni_3Cl_2(OH)_4$ and (b) Try-Ni-MOF.

Fig. S8. Raman spectra of a) GO, GA and AZ-GA and b) $Ni_3Cl_2(OH)_4$ and Try-Ni-MOF samples.

Fig. S9. TGA curves of (a) GO, GA and Az-GA and (b) $Ni_3Cl_2(OH)_4$ and Try-Ni-MOF samples in air at a heating rate of 5 °C min^{-1}.

Fig. S10. Suggested mechanism for electrochemical oxidation of (A) Az to B, C or D compounds.

Fig. S11. (a) CVs of the Az-GA electrodes with different azure A to GO ratios from 0.04 to 1 wt% at scan rate of 10 mV s^{-1} and (b) change in specific capacitance as a function of the wt% azure A to GO ratios for Az-GA/NF electrodes.

Fig. S12. CVs of $Ni_3Cl_2(OH)_4$/NF electrode in three-electrode cell setup in aqueous 3.0 m KOH electrolyte at various scan rates from 5 to 100 mV s^{-1}.

Fig. S13. (a) CVs of the Try-Ni-MOF electrodes with different $NiCl_2.6H_2O$ to trypan blue ratios (1:1, 1:2, 1:4, 1:5, and 1:6) at scan rate of 10 mV s^{-1} and (b) change in specific capacitance as a function of the $NiCl_2.6H_2O$ to trypan blue ratios for Try-Ni-MOF/NF electrodes.

Fig. S14. (a and c) the voltammetric charge (c) versus scan rate ($\nu^{-1/2}$) and (b and d) $1/c(\nu)$ versus $\nu^{1/2}$ plots for Az-GA/NF and Try-Ni-MOF/NF electrode, according to Trasatti method.

Fig. S15. (a, d) GCD of the GA/NF and $Ni_3Cl_2(OH)_4$/NF electrodes at different current densities in an aqueous 3.0 M KOH electrolyte, (b, e) long-term cycling stability of the GA/NF, Az-GA/NF, $Ni_3Cl_2(OH)_4$/NF, and Try-Ni-MOF/NF electrodes over 5000 cycles at a current density of 10 A g^{-1} in an aqueous 3.0 M KOH electrolyte, and (c, f) Bode plots (log $|Z|$ vs. log frequency and phase angle vs. log frequency) for the GA/NF, Az-GA/NF, $Ni_3Cl_2(OH)_4$/NF, and Try-Ni-MOF/NF electrodes at a frequency range from 100 KHz to 10 mHz, respectively.

Fig. S16. Equivalent circuit models used to fit the experimental EIS data of the (a) GA/NF and Az-GA/NF and (b) $Ni_3Cl_2(OH)_4$/NF and Try-Ni-MOF/NF electrodes in a three-electrode system and in an aqueous 3.0 M KOH electrolyte, respectively.

Fig. S17. (a) Az-GA (negative pole) and Try-Ni-MOF (positive pole) electrodes measured at a scan rate of 10 mV s^{-1} in three-electrode configurations, (b) CV curves of the Az-GA//Try-Ni-MOF asymmetric device at different potential windows 10 mV s^{-1}, (c) GCDs of a Az-GA//Try-Ni-MOF asymmetric device at different potential windows, and (d) specific capacitances of Az-GA//Try-Ni-MOF asymmetric device at various current densities.

Table S1. The d-spacing and crystallite size of GO, GA, Az-GA, $Ni_3Cl_2(OH)_4$, and Try-Ni-MOF.

Table S2. Comparison of the electrochemical performances of the Az-GA electrode with other anode electrode reported literatures.

Table S3. Comparison of the electrochemical performances of the Try-Ni-MOF electrode with other cathode electrode reported literatures.

Table S4. Values of equivalent circuit parameters for the GA and Az-GA electrodes.

Table S5. Values of equivalent circuit parameters for the $Ni_3Cl_2(OH)_4$ and Try-Ni-MOF electrodes.

Table S6. Comparison of the electrochemical performances of the Az-GA//Try-Ni-MOF device with other devices.

Videos S1

Films.m4v , Film 2.m4v

Characterization of materials

Bragg equation: $n\lambda = 2d \sin(\theta)$

where, n is the order of reflection and can be small integers (number of crystal pages), λ is the wavelength of the X-ray that moves the electron or neutron, d is the empty space between atoms, ɵ is the angle at which the reflected beams have the greatest amplitude with respect to the initial beams.

Scherrer equation: $D = K\lambda/(B \cos\theta)$

Where D is the mean size of the ordered (crystalline) domains, K is a dimensionless shape factor, with a value close to unity (about 0.9), λ is the X-ray wavelength, β is the line broadening at half the maximum intensity (FWHM), after subtracting the instrumental line broadening, in radians, θ is the Bragg angle.

Bragg equation: nλ =2d sin(ɵ)

where, n is the order of reflection and can be small integers (number of crystal pages), λ is the wavelength of the X-ray that moves the electron or neutron, d is the empty space between atoms, ɵ is the angle at which the reflected beams have the greatest amplitude with respect to the initial beams.

Scherrer equation: D = Kλ/(B cosθ)

Where D is the mean size of the ordered (crystalline) domains, K is a dimensionless shape factor, with a value close to unity (about 0.9), λ is the X-ray wavelength, β is the line broadening at half the maximum intensity (FWHM), after subtracting the instrumental line broadening, in radians, θ is the Bragg angle.

Reactions:

The urea was hydrolyzed into NH_4^+, OH^- and CO_2 during the hydrothermal process (**Reaction 1**). Then, the resulting NH_4^+, OH^- reacted with $NiCl_2$ to formed porous $Ni_3Cl_2(OH)_4$ nanosheets (**Reaction 2**). According to the **Reaction 3**, it can be noted that the pseudocapacitive behavior of the compound is mainly attributed to the oxidation and reduction properties of Ni^{2+} and Ni^{3+}. The CVs (**Fig. S12**) show the redox behavior of $Ni_3Cl_2(OH)_4$/NF electrode and reduction of Ni^{2+}.

$CO(NH_2)_2 + 3H_2O \rightarrow 2NH_4^+ + 2OH^- + CO_2$ **Reaction 1**

$Ni^{2+} + Cl^- + OH^- \rightarrow Ni_3Cl_2(OH)_4$ **Reaction 2**

$Ni^{2+} \rightarrow Ni^{3+} + e^-$ **Reaction 3**

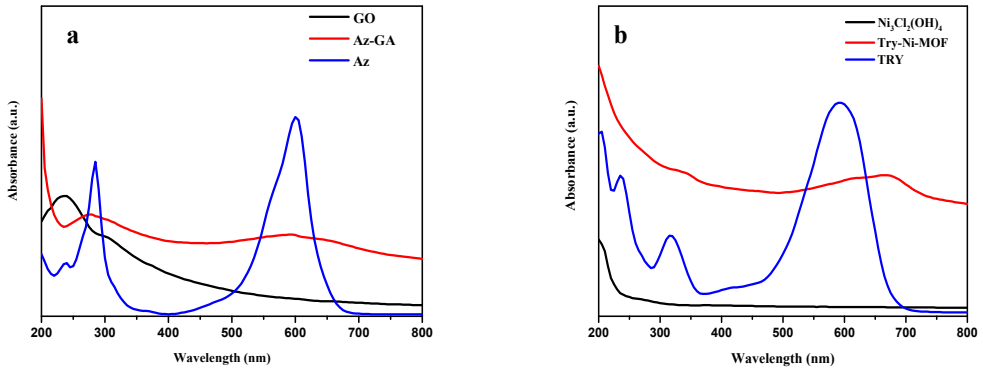

Fig. S1. UV-vis absorption of (a) pure Az, GO, Az/GO and (b) Try, $Ni_3(Cl)_2(OH)_4$ and Try-Ni-MOF aqueous solutions.

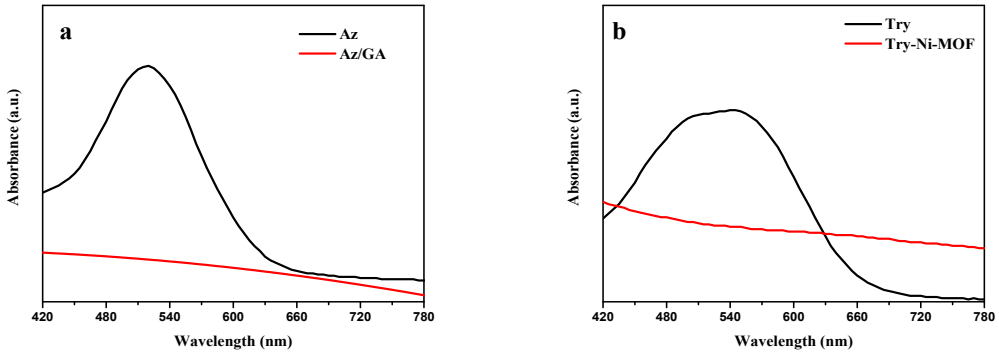

Fig. S2. UV-vis. absorption spectra of (a) pure azure A and Az/GA and (b) pure trypan blue and Try-Ni-MOF in 3.0 M KOH solution using three electrode cell setup after completing 500 galvanostatic charge-discharge cycles, respectively.

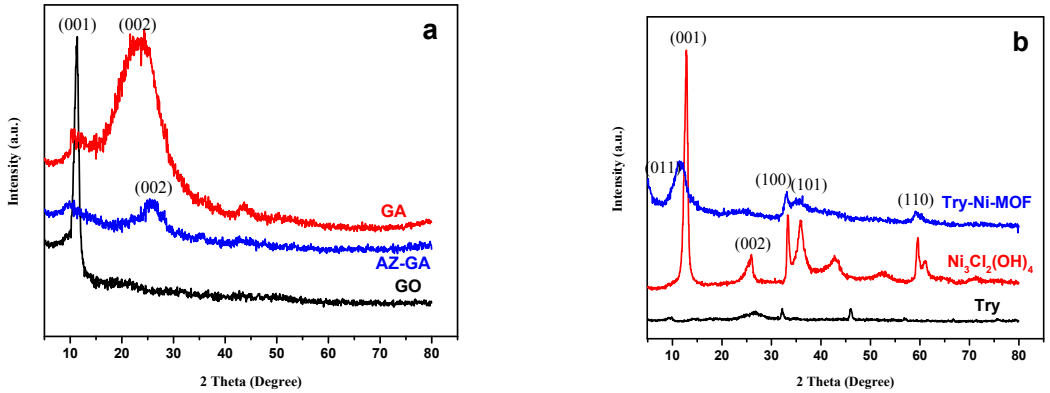

Fig. S3. XRD patterns of (a) GO, GA, and Az–GA and (b) Try, $Ni_3Cl_2(OH)_4$, and the Try–Ni-MOF.

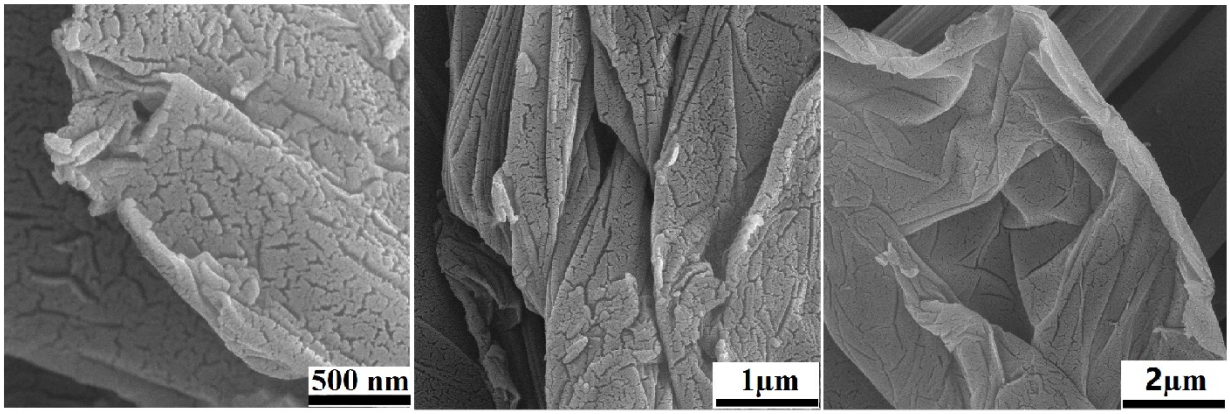

Fig. S4. SEM images of GO

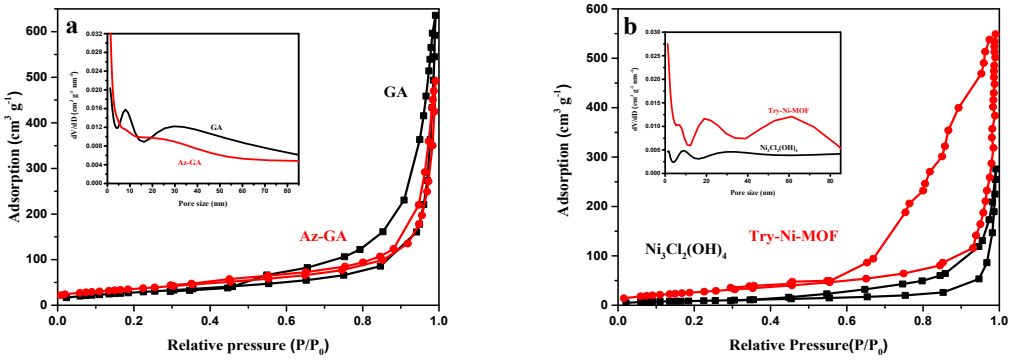

Fig. S5. N2 adsorption/desorption isotherms of the (a) GA and Az-GA, and (b) $Ni_3Cl_2(OH)_4$ and Try-Ni-MOF samples. The insets are BJH pore size distribution curves.

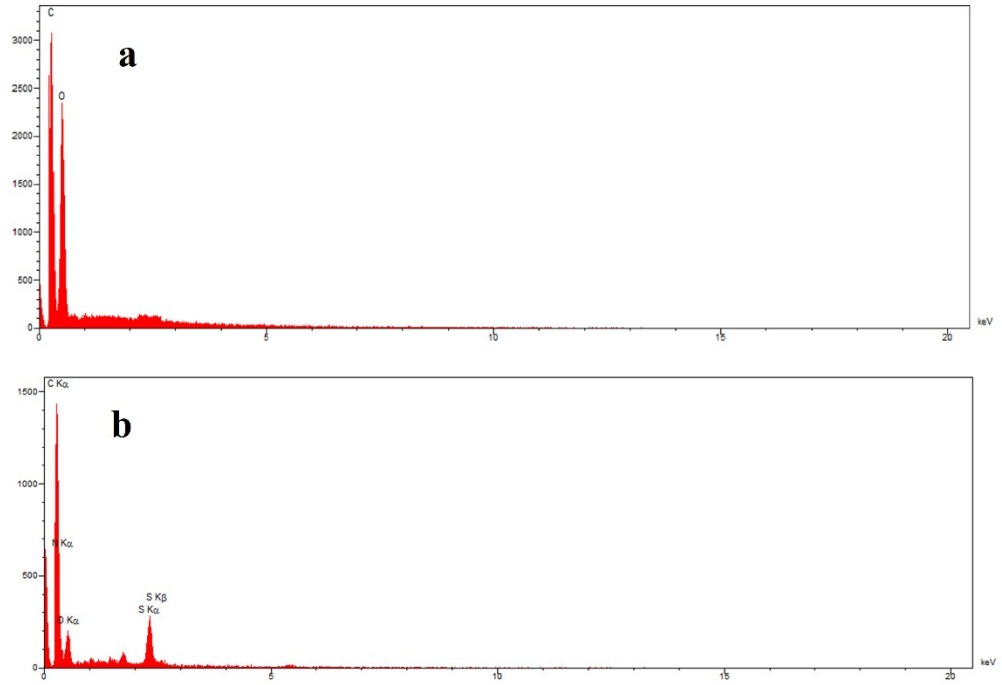

Fig. S6. EDS spectra of the (a) GO and (b) Az-GA

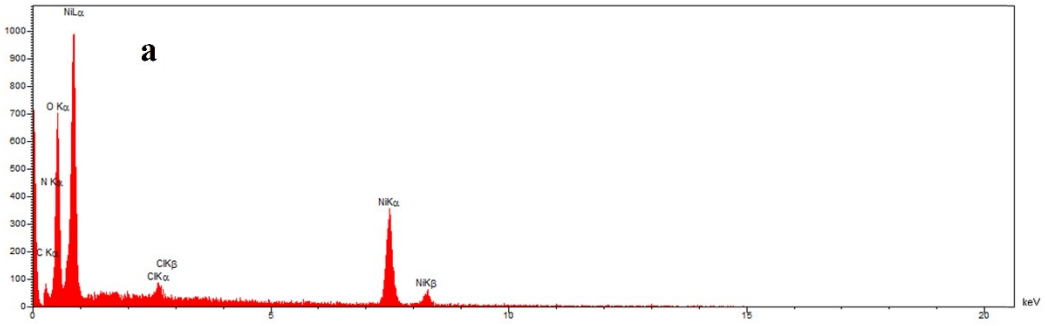

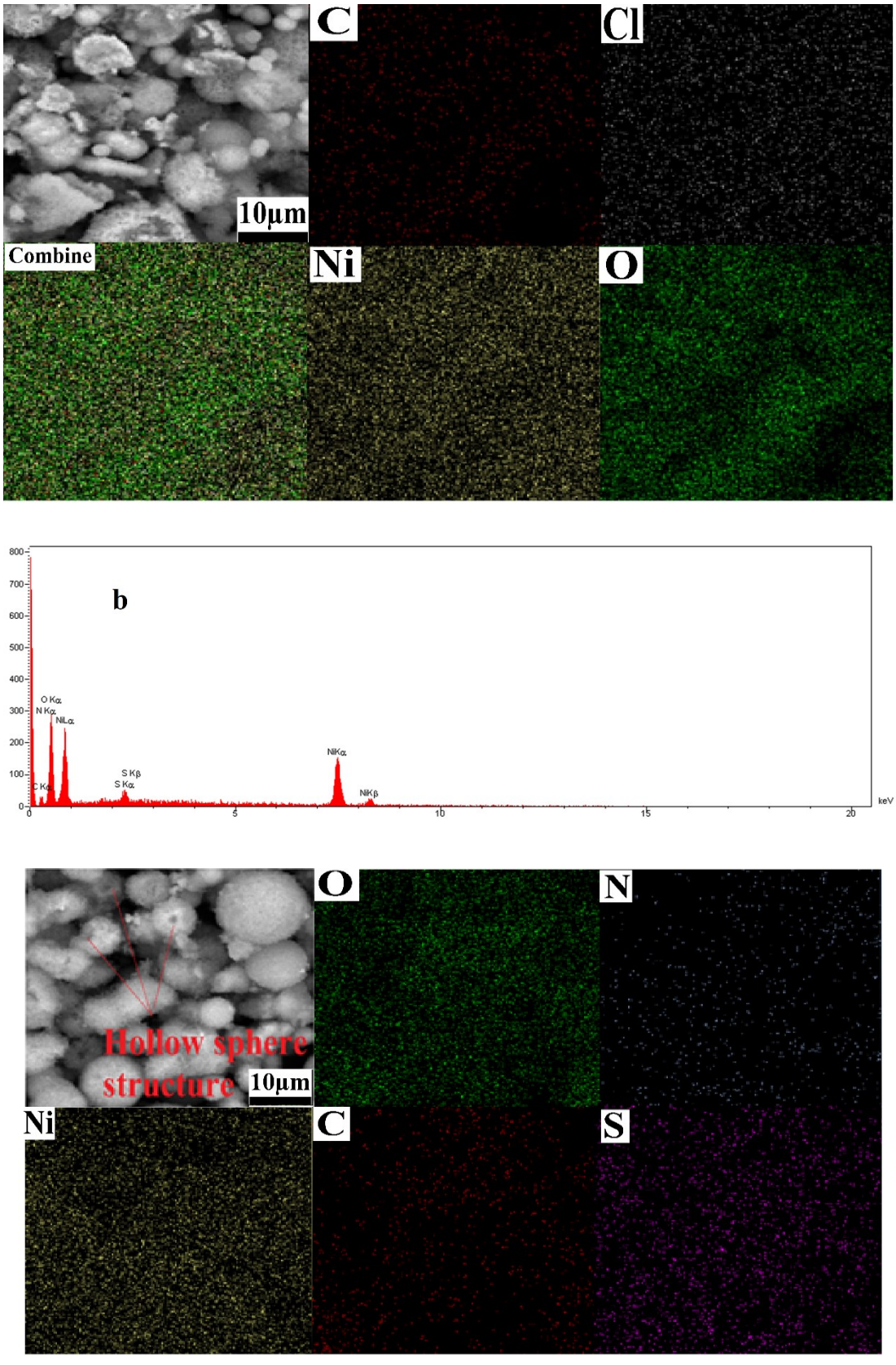

Fig. S7. EDS spectra and mapping of the (a) $Ni_3Cl_2(OH)_4$ and (b) Try-Ni-MOF.

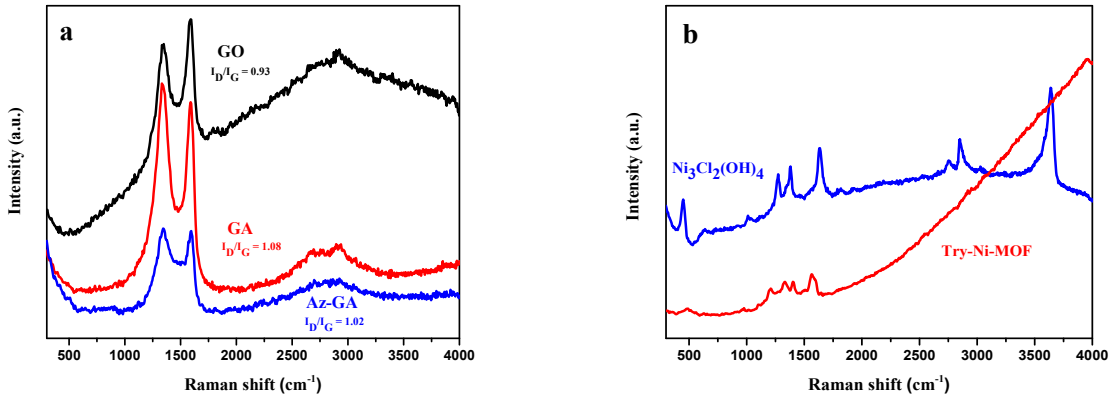

Fig. S8. Raman spectra of a) GO, GA and AZ-GA and b) $Ni_3Cl_2(OH)_4$ and Try-Ni-MOF samples.

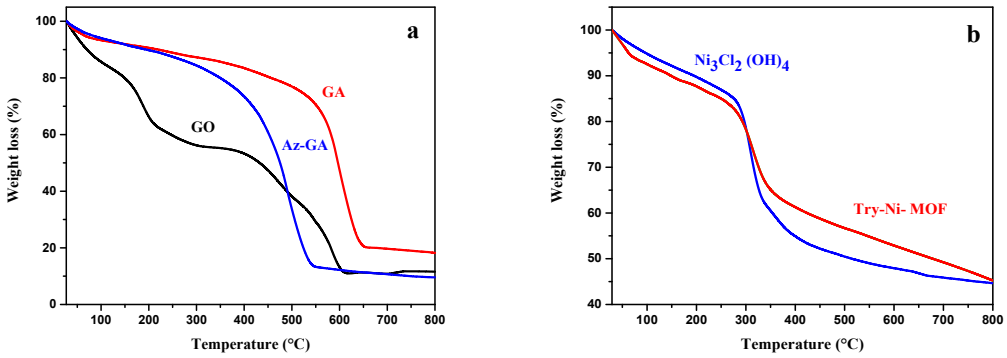

Fig. S9. TGA curves of (a) GO, GA and Az-GA and (b) $Ni_3Cl_2(OH)_4$ and Try-Ni-MOF samples in air at a heating rate of 5 °C min^{-1}.

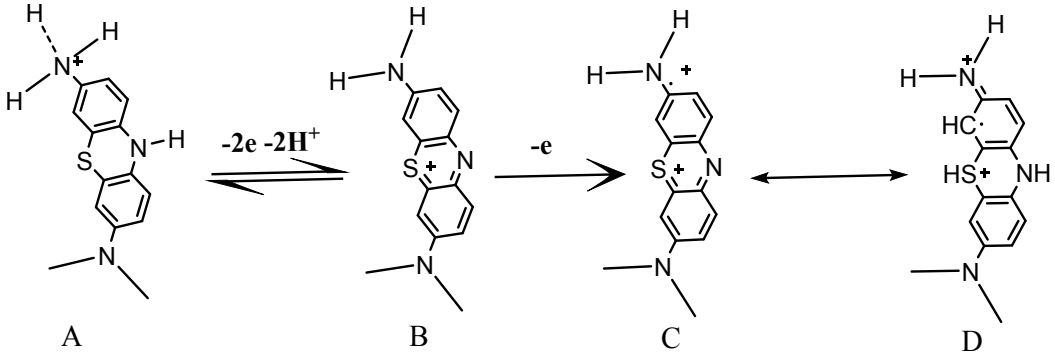

Fig. S10. Suggested mechanism for electrochemical oxidation of (A) Az to B, C or D compounds.

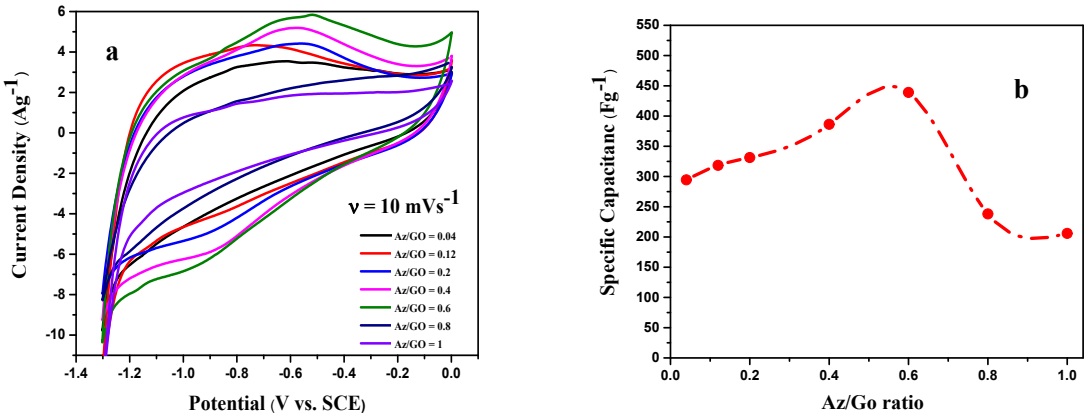

Fig. S11. (a) CVs of the Az-GA electrodes with different azure A to GO ratios from 0.04 to 1 wt% at scan rate of 10 mV s^{-1} and (b) change in specific capacitance as a function of the wt% azure A to GO ratios for Az-GA/NF electrodes.

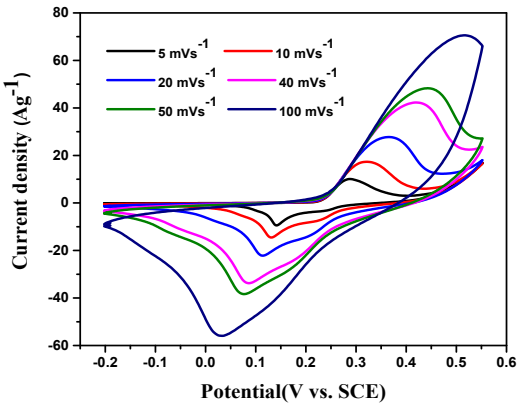

Fig. S12. CVs of $Ni_3Cl_2(OH)_4$/NF electrode in three-electrode cell setup in aqueous 3.0 m KOH electrolyte at various scan rates from 5 to 100 mV s^{-1}.

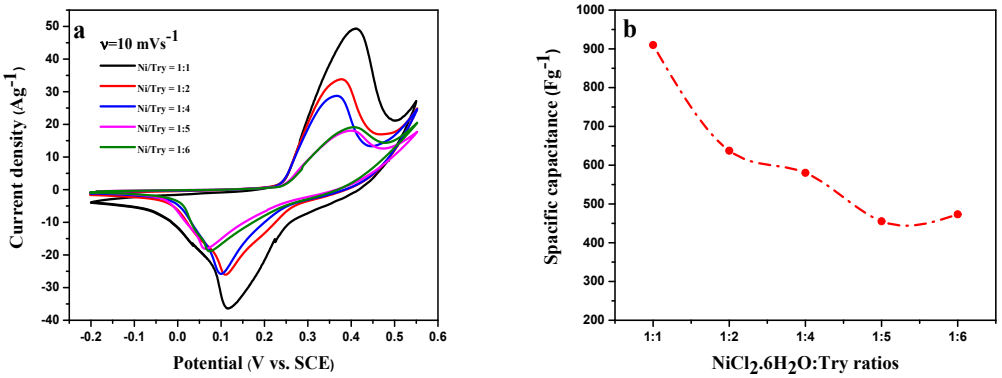

Fig. S13. (a) CVs of the Try-Ni-MOF electrodes with different $NiCl_2.6H_2O$ to trypan blue ratios (1:1, 1:2, 1:4, 1:5, and 1:6) at scan rate of 10 mV s^{-1} and (b) change in specific capacitance as a function of the $NiCl_2.6H_2O$ to trypan blue ratios for Try-Ni-MOF/NF electrodes.

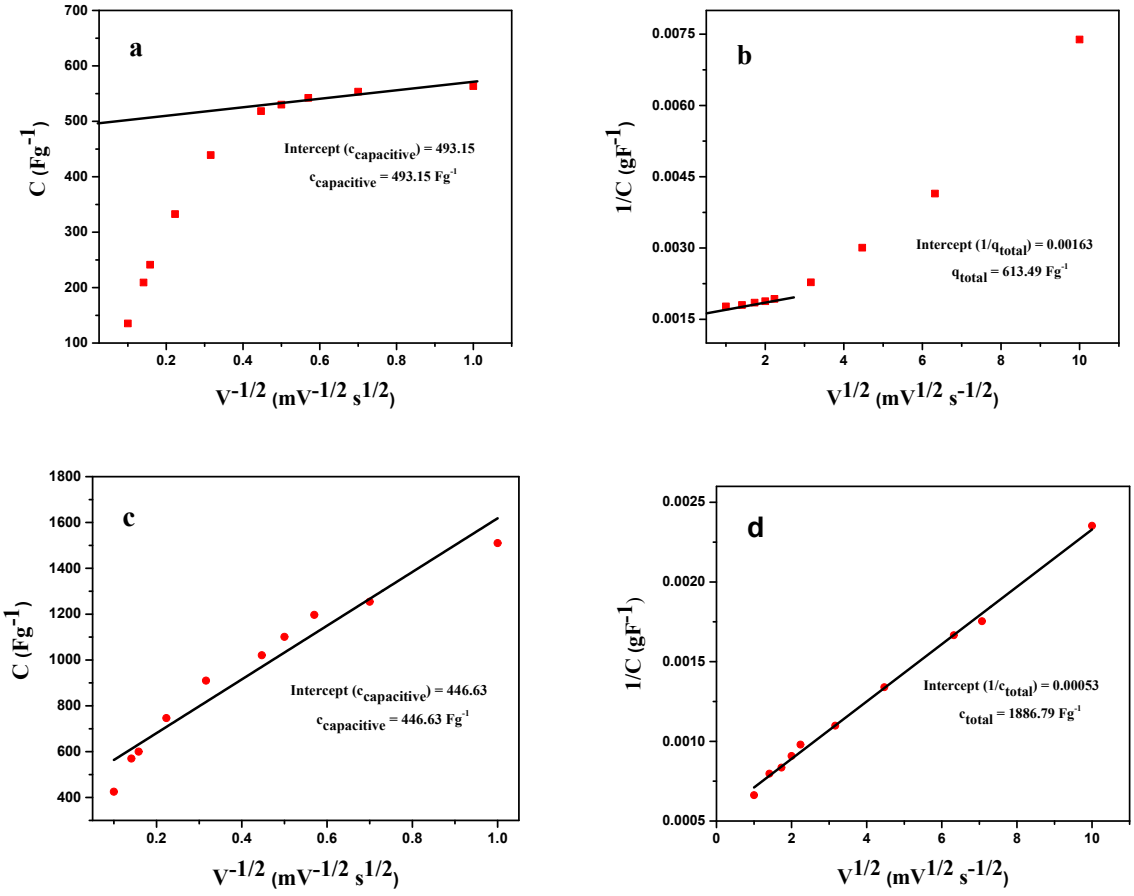

Fig. S14. (a and c) the voltammetric charge (c) versus scan rate ($\nu^{-1/2}$) and (b and d) $1/c(\nu)$ versus $\nu^{1/2}$ plots for Az-GA/NF and Try-Ni-MOF/NF electrode, according to Trasatti method.

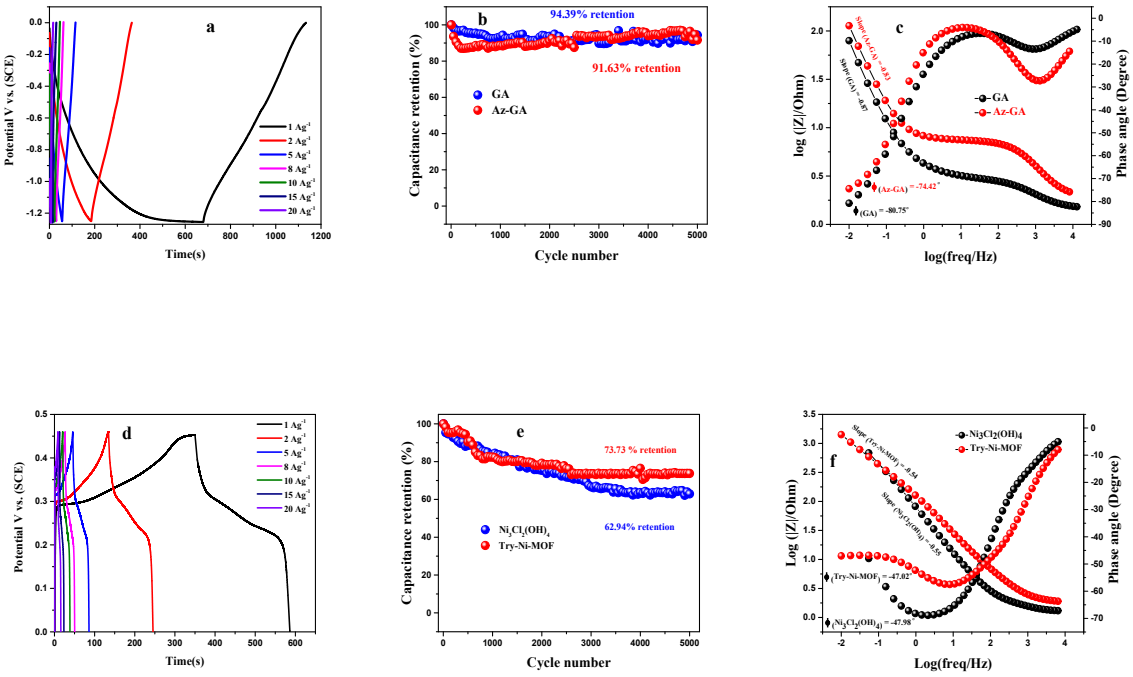

Fig. S15. (a, d) GCD of the GA/NF and $Ni_3Cl_2(OH)_4$/NF electrodes at different current densities in an aqueous 3.0 M KOH electrolyte, (b, e) long-term cycling stability of the GA/NF, Az-GA/NF, $Ni_3Cl_2(OH)_4$/NF, and Try-Ni-MOF/NF electrodes over 5000 cycles at a current density of 10 A g^{-1} in an aqueous 3.0 M KOH electrolyte, and (c, f) Bode plots (log $|Z|$ vs. log frequency and phase angle vs. log frequency) for the GA/NF, Az-GA/NF, $Ni_3Cl_2(OH)_4$/NF, and Try-Ni-MOF/NF electrodes at a frequency range from 100 KHz to 10 mHz, respectively.

a

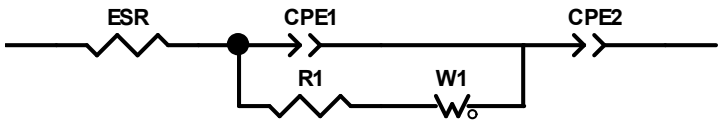

b

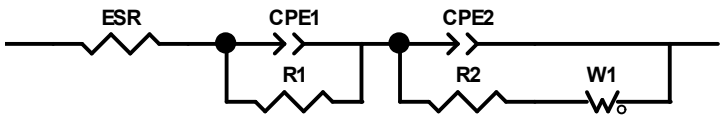

Fig. S16. Equivalent circuit models used to fit the experimental EIS data of the (a) GA/NF and Az-GA/NF and (b) $Ni_3Cl_2(OH)_4$/NF and Try-Ni-MOF/NF electrodes in a three-electrode system and in an aqueous 3.0 M KOH electrolyte, respectively.

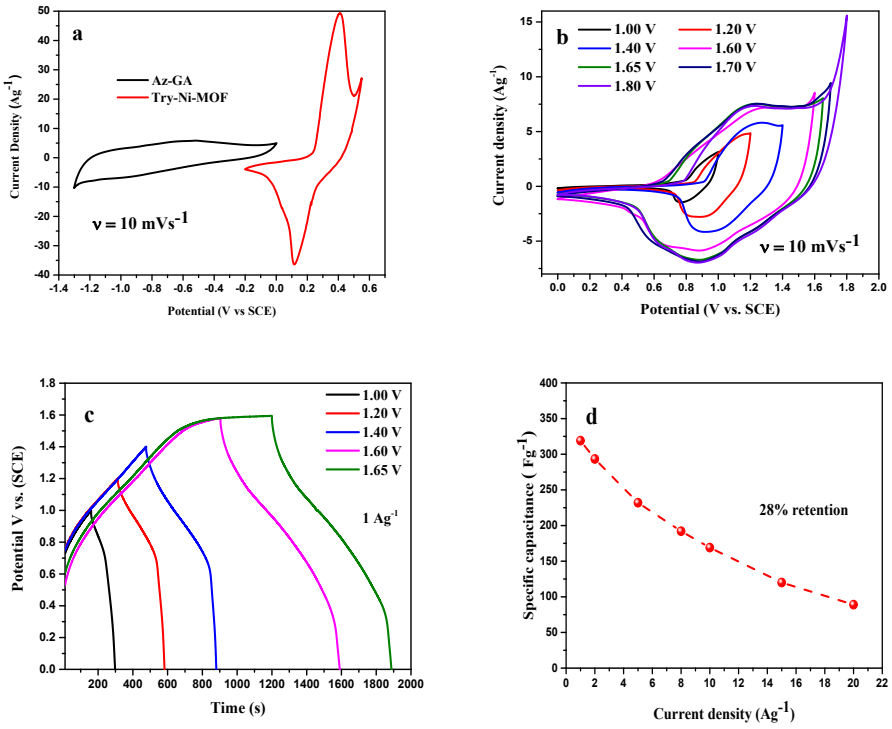

Fig. S17. (a) Az-GA (negative pole) and Try-Ni-MOF (positive pole) electrodes measured at a scan rate of 10 mV s^{-1} in three-electrode configurations, (b) CV curves of the Az-GA//Try-Ni-MOF asymmetric device at different potential windows 10 mV s^{-1}, (c) GCDs of a Az-GA//Try-Ni-MOF asymmetric device at different potential windows, and (d) specific capacitances of Az-GA//Try-Ni-MOF asymmetric device at various current densities.

Table S1 The d-spacing and crystallite size of GO, GA, Az-GA, $Ni_3Cl_2(OH)_4$, and Try-Ni-MOF.

Dataset Name	Pos. [θ]	Height [cts]	FWHM Left [θ.]	d-spacing [Å]	d- mean size [nm]
GO	11.36(9)	2688.85	1.200	7.84613	-
GA	24.36(2)	2056.6	0.64	3.65065	-
Az-GA	26.41(1)	585.0	0.7230	3.38550	-
$Ni_3Cl_2(OH)_4$	12.8784	7976.82	0.3936	6.87422	5-11
Try-Ni-MOF	11.588(9)	1184(16)	2.79(2)	7.63027	2-5

Table S2. Comparison of the electrochemical performances of the Az-GA electrode with other anode electrode reported literatures.

Electrode material	**Areal capacitance/ capacity (F cm^{-2}/mA h cm^{-2})**	**Specific capacitance/ capacity (F g^{-1}/mA h g^{-1})**	**Current load**	**Electrolyte**	**Stability (Cycles)**	**Ref.**
$NiCo_2O_4$/GH/NF composite	3.84 F cm^{-2}	3428 F g^{-1}	2 mA cm^{-2}	0.008 M $NiCl_2.6H_2O$, 0.016 M $CoCl_2.6H_2O$, and 0.1 M Na_2SO_4	-	[1]
FGS[a]-SSG[b]/PANI	1.36 F cm^{-2}	491.3 F g^{-1}	0.5 A g^{-1}	1.0 M H_2SO_4	86% at 50 mVs^{-1} (3,000)	[2]
Fe_3O_4/graphene nanocomposites	-	300 F g^{-1}	0.4 A g^{-1}	1.0 M KOH	93% at 0.4 A g^{-1} (500 cycles)	[3]
SG[c]/PANI	-	478 F g^{-1}	0.5 A g^{-1}	1.0 M H_2SO_4	88% at	[4]

nanocomposite papers					0.5 A g^{-1} (2,000)	
Th–GA[d] nanocomposite	-	512 F g^{-1}	1 A g^{-1}	1.0 M H_2SO_4	82% at 1 A g^{-1} (6,000)	5
Graphene encapsulated NiS/Ni_3S_4 (NSG) nanostructure	-	827 F g^{-1}	5 A g^{-1}	6.0 M KOH	88% at 5 A g^{-1} (5,000)	6
3-D GPCN nanosheets[e]	-	316.8 F g^{-1}	1 A g^{-1}	1.0 M KOH	92.5% at 1 A g^{-1} (2,000)	7
MnO_2/VGNs[f]/Ni hybrid	186 mFcm^{-2}	-	1 mA cm^{-2}	0.1 M $MnSO_4$ and 1 M Na_2SO_4	60% at 100 mVs^{-1} (10,000)	8
RGO/Ni_3S_2/MoS_2 composite	6451 mF·cm^{-2}	-	40 mA·cm^{-2}	2.0 M KOH	87.2% at 110 mA·cm^{-2} (5,000)	9
NiFe/rGO	-	1224 F g^{-1}	10 mVs^{-1}	1.0 M KOH	89% at 10 mVs^{-1} (2,000)	10
GA[g]@NF	-	366 F g^{-1}	2 A g^{-1}	6.0 M KOH	60% at 10 A g^{-1} (2,000)	11
Az-GA	-	716.06 F g^{-1}	1 A g^{-1}	3.0 M KOH	94.39% at 10 A g^{-1} (5,000)	This work

[a] FGS : Flexible graphite sheet, [b] SSG : Self-supporting graphene, [c] SG :Sulfonate graphene, [d] Th–GA : Thionine–Graphene aerogel, [e] 3-D GPCN nanosheets : Three-dimensional graphene-like porous carbon nanosheets, [f] VGNs : Vertical graphene nanosheets, [g] GA : Graphene aerogel

Table S3. Comparison of the electrochemical performances of the Try-Ni-MOF electrode with other cathode electrode reported literatures.

Electrode material	Areal capacitance / capacity ($F\ cm^{-2}$/mA h cm^{-2})	Specific capacitance/ capacity ($F\ g^{-1}$/mA h g^{-1})	Current load	Electrolyte	Stability (Cycles)	Ref.
$Ni_{4.5}Co_{4.5}S_8$ (Ni battery)	-	206 mAh g^{-1}	1 A g^{-1}	4.0 M KOH	95% at 20 A g^{-1} (5,000)	12
$Ni(OH)_2$/NG[a] (Ni battery)		230 mAh g^{-1}	1 A g^{-1}	1.0 M KOH	93% at 10 mV^{-1} (1,000)	13
$LiNi_{0.5}Mn_{1.5}O_4$ (Li-ion battery)	-	144 mAh g^{-1}	150 mA g^{-1}	LiPF6 in Ethylene carbonate and dimethyl carbonate	90% at 300 mA g^{-1} (250)	14
Ni-MH (Ni battery)	-	276 mAh g^{-1}	0.1 C (1 C=183.6 mA g^{-1})	PVA/ KOH	-	15
NiO@ Ni Micro/nanostructures	92.4 mF cm^{-2}	-	1 mA cm^{-2}	2.0 M KOH	100% at 4 A g^{-1} (1,500)	16
$NiO/CuO_{-0.3}/GO_{-30}$ composites	-	1451 F g^{-1}	1 A g^{-1}	6.0 M KOH	82.95% at 10 A g^{-1} (1,000)	17
$(Co(OH)_2/Co_9S_8)$ @ NiTe/Ni composite	5.28 F cm^{-2}	-	10 mA cm^{-2}	6.0 M KOH	87.80% at 50 A g^{-1} (10,000)	18
Ni–Co–S/NF nanosheet	-	1406.9 F g^{-1}	0.5 A g^{-1}	1.0 M KOH	88.6% at 10 A g^{-1} (1,000)	19
NiO	-	523 F g^{-1}	1 A g^{-1}	6.0 M KOH	77.25% at 10 A g^{-1} (1,000)	17
Co^{2+}/Co^{3+}- doped $Ni(OH)_2$ branched	-	999 F g^{-1}	2 A g^{-1}	3.0 M	82% at	20

nanosheets-interlaced structure				KOH	10 A g^{-1} (7,000)	
2D N-NiO UTNSs[b]	-	540 F g^{-1}	1 A g^{-1}	1.0 M KOH	85% at 10 A g^{-1} (10,000)	[21]
NiCoP/NPC HFSs[c] composite	-	660.3 F g^{-1}	1 A g^{-1}	3.0 M KOH	85% at 6 A g^{-1} (2,000)	[22]
Try-Ni-MOF	-	845.43 F g^{-1}	1 A g^{-1}	3.0 M KOH	73.73% at 10 A g^{-1} (5,000)	This work

[a] NG : Nitrogen-doped graphene, [b] 2D N-NiO UTNSs : 2D N-doped NiO ultrathin nanosheets, [c] NPC HFSs: N and P atoms with hollow and fold-sphere, [c] :

.....

Table S4. Values of equivalent circuit parameters for the GA and Az-GA electrodes

Sample	**ESR (Ω)**	**R_{ct1} (Ω)**	**CPE_1 (Fs^{n-1})**	**n_1**	**W (Ω $s^{-1/2}$)**	**CPE_2 (Fs^{n-1})**	**n_2**
GA	1.45	1.44	1.4×10^{-3}	0.75	0.27	0.26	0.92
Az-GA	1.87	5.50	0.27×10^{-3}	0.81	0.32	0.11	0.90

Table S5. Values of equivalent circuit parameters for the $Ni_3Cl_2(OH)_4$ and Try-Ni-MOF electrodes

Sample	**ESR (Ω)**	**R_{ct1} (Ω)**	**CPE_1 (Fs^{n-1})**	**n_1**	**W (Ω $s^{-1/2}$)**	**R_{ct2} (Ω)**	**CPE_2 (Fs^{n-1})**	**n_2**
$Ni_3Cl_2(OH)_4$	1.27	0.31	1.3×10^{-3}	0.80	1.02	1336	2.7×10^{-3}	0.80
Try-Ni-MOF	1.78	1.58	2.5×10^{-3}	0.82	0.50	248	1.5×10^{-3}	0.75

Table S6. Comparison of the electrochemical performances of the Az-GA//Try-Ni-MOF device with other devices.

Device (Type)	Capacity (mAh g^{-1})	Capacitance (F g^{-1})	Specific energy (Wh kg^{-1}) at specific power (kW kg^{-1})	Specific power (kW kg^{-1}) at specific energy (Wh kg^{-1})	Cycles	Capacity retention	Electrolyte	Ref.
ZCNM-NS[a]//AC [b] (battery-supercapacitor hybrid)	-	71.3 at 5 mA cm^{-2}	25.3 at 0.787	9.4 at 18.4	5,000	81.5% at 10 mA cm^{-2}	2.0 M KOH	23
rG/NCS/NCO[c]//rGO (Asym. supercapacitor)	-	104 at 3 Ag^{-1}	32 at 0.375	-	1,000	82 % at 30 A g^{-1}	PVA-KOH	24
$Co(OH)_2$–$MoSe_2$//AC (Asym. supercapacitor)	-	99 at 1 Ag^{-1}	30.12 at 0.985	12.2 at 18.28	3,000	86.2% at 10 A g^{-1}	6.0 M KOH	25
$ZnFe_2O_4$//$Ni(OH)_2$ (Asym. supercapacitor)	-	93 at 0.6 mA cm^{-2}	33 at 0.068	0.209 at 14	1,000	88% at 1 $mAcm^2$	6.0 M KOH	26
Pd-GA//$Ni(OH)_2$ (Ni superbattery)	190 at 0.2 A g^{-1}	429 at 0.2 A g^{-1}	185.7 at 38.8×10^{-3}	11.3 at 30.3	1,000	54% at 4 A g^{-1}	6.0 M KOH	27
PCO//3DPG (pseudocapacitive)	-	229 at 2 A g^{-1}	71.58 at 1.5	-	2000	95% at 50 mV s^{-1}	6.0 M KOH	28
AC//$LiNi_{0.5}Mn_{1.5}O_4$ (Li-ion capacitor)	-	124 at 100 mA g^{-1}	19 at 0.150	2.5 at 8.0	3,000	81% at 1 A g^{-1}	1.0 M $LiPF_6$	14
$NiCoMoS_x$//AC (Asym. Supercapacitor)	-	136 at 1 A g^{-1}	48.2 at 0.807	-	10,000	91.6% at 1 A g^{-1}	3.0 M KOH	29

CoNi-MOF//AC (Asym. Supercapacitor)	-	-	28.5 at 1.5	-	5,000	94% at 1 A g^{-1}	1.0 M KOH	[30]
HCO-PFC[d]//FG[f] full cell	1960 at 3 mA cm^{-2}	1633 at 3 mA cm^{-2}	79.54 at 0.778	-	5,000	81% at 20 A g^{-1}	6 m KOH + 0.06 m PFC	[31]
GON[e]//RGO (Asym. Supercapacitor)	-	-	40.5 at 0.900	8.526 at 9.5	5,000	87% at 10 A g^{-1}	PVA/KOH	[32]
Fe_3C/CF//$Ni_{4.5}Co_{4.5}$-selenide nanowires/NPCC (Battery-supercapacitor)	-	113.7 at 1 A g^{-1}	47.4 at 1.5	-	4,000	80% at 10 **A g^{-1}**	PVA/KOH	[33]
Ni_3S_2/NiV-LDH/rGO/NF//AC (Asym. Supercapacitor)	-	-	59.4 at 0. 852	-	8,000	98.3% at 2 A g^{-1}	2.0 M KOH	[34]
Cd-GA//$Ni(OH)_2$ (Ni superbattery)	50 at 0.15 A g^{-1}	-	51.7 at 100 mA g^{-1}	5.4 at 7.8	1,000	88% at 6 A g^{-1}	6.0 M KOH	[27]
GM-LEG[g] @NiCo-MOF//AC	-	3250 at 7.5 A g^{-1}	76.3 at 2.25	-	-	-	3.0 M KOH + 0.1 M $K_4[Fe(CN)_6]$	[35]
Az-GA//Try-Ni-MOF (Asym. supercapatteries)	-	319 at 1 A g^{-1}	66.55 at 0.349	4.5 at 11.11	5,000	92.12% at 10 A g^{-1}	3.0 M KOH	This work

[a] ZCNM-NS : $ZnCo_2O_4$@$NiMoO_4$ core-shell nanosheets, [b] AC: activated carbon, [c] NCS/NCO: $NiCo_2S_4$@$NiCo_2O_4$ core@shell nanoneedle, [d] PFC : potassium ferricyanide, [f] FG: Fe_2O_3/graphene, [e] GON: nitrogen grafted graphene oxinitride, [g] LEG : liquid-phase exfoliated graphene

References

1 H. Yao, F. Zhang, G. Zhang and Y. Yang, *Electrochim. Acta*, 2019, **294**, 286–296.

2 G. Xin, Y. Wang, X. Liu, J. Zhang, Y. Wang, J. Huang and J. Zang, *Electrochim. Acta*, 2015, **167**, 254–261.

3 J. Liao, Y. Li, Z. Wang, L. Lv and L. Chang, *Mater. Chem. Phys.*, 2021, **258**, 123995.

4 T. Fan, S. Tong, W. Zeng, Q. Niu, Y. Liu, C. Y. Kao, J. Liu, W. Huang, Y. Min and A. J. Epstein, *Synth. Met.*, 2015, **199**, 79–86.

5 Y. Shabangoli, M. S. Rahmanifar, M. F. El-Kady, A. Noori, M. F. Mousavi and R. B. Kaner, *Adv. Energy Mater.*, 2018, **8**, 1–12.

6 S. Nandhini and G. Muralidharan, *Electrochim. Acta*, 2021, **365**, 137367.

7 Z. Li, L. Zhang, X. Chen, B. Li, H. Wang and Q. Li, *Electrochim. Acta*, 2019, **296**, 8–17.

8 Y. Zhou, X. Cheng, F. Huang, Z. Sha, Z. Han, J. Chen, W. Yang, Y. Yu, J. Zhang, S. Peng, S. Wu, A. Rider, L. Dai and C. H. Wang, *Carbon N. Y.*, 2021, **172**, 272–282.

9 W. Wei, B. Liu, Y. Gan, H. Ma, D. Chen, J. Qi and S. Li, *Surf. Coatings Technol.*, , DOI:10.1016/j.surfcoat.2020.126442.

10 S. Azizi, M. Seifi and M. B. Askari, *Phys. B Condens. Matter*, 2021, **600**, 412606.

11 S. Ye, J. Feng and P. Wu, *ACS Appl. Mater. Interfaces*, 2013, **5**, 7122–7129.

12 H. Khani and D. O. Wipf, *ACS Appl. Mater. Interfaces*, 2017, **9**, 6967–6978.

13 X. Wu, H. Bin Wu, W. Xiong, Z. Le, F. Sun, F. Liu, J. Chen, Z. Zhu and Y. Lu, *Nano Energy*, 2016, **30**, 217–224.

14 N. Arun, A. Jain, V. Aravindan, S. Jayaraman, W. Chui Ling, M. P. Srinivasan and S. Madhavi, *Nano Energy*, 2015, **12**, 69–75.

15 Z. Ren, J. Yu, Y. Li and C. Zhi, *Adv. Energy Mater.*, 2018, **8**, 1–12.

16 S. Wang, H. Liu, J. Hu, L. Jiang, W. Liu, S. Wang, S. Zhang, J. Yin and J. Lu, *Appl. Surf. Sci.*, 2020, 148216.

17 H. Xie, J. Li, C. Chen, F. Dang and Y. He, *Mater. Lett.*, 2021, **282**, 128887.

18 B. Wu, F. Zhang, Z. Nie, H. Qian, P. Liu, H. He, J. Wu, Z. Chen and S. Chen, *Electrochim. Acta*, 2021, **365**, 137325.

19 K. Tao, X. Han, Q. Ma and L. Han, *Dalt. Trans.*, 2018, **47**, 3496–3502.

20 J. Wang, J. Li, Y. Liu, M. Wang and H. Cui, *J. Mater. Sci.*, 2021, **56**, 3011–3023.

21 J. Xue, S. Wang, H. Zhang, Y. Song, Y. Li and J. Zhao, *J. Mater. Sci. Mater. Electron.*, , DOI:10.1007/s10854-020-04581-3.

22 M. Yi, B. Lu, X. Zhang, Y. Tan, Z. Zhu, Z. Pan and J. Zhang, *Appl. Catal. B Environ.*, 2021, **283**, 119635.

23 Y. Meng, D. Yu, Y. Teng, H. Qi, X. Liu, Y. Wu, X. Zhao and X. Liu, *J. Energy Storage*, 2020, **29**, 101195.

24 A. Singh, S. K. Ojha, M. Singh and A. K. Ojha, *Electrochim. Acta*, 2020, **349**, 136349.

25 A. Alam, G. Saeed and S. Lim, *J. Electroanal. Chem.*, 2020, **879**, 114775.

26 A. Shanmugavani and R. K. Selvan, *RSC Adv.*, 2014, **4**, 27022–27029.

27 Y. Shabangoli, M. F. El-Kady, M. Nazari, E. Dadashpour, A. Noori, M. S. Rahmanifar, X. Lv, C. Zhang, R. B. Kaner and M. F. Mousavi, *Small*, 2020, **16**, 1–12.

28 28 T. Zhai, L. Wan, S. Sun, Q. Chen, J. Sun, Q. Xia and H. Xia, *Adv. Mater.*, 2017, **29**, 1–8.

29 W. Yang, H. Guo, L. Yue, Q. Li, M. Xu, L. Zhang, T. Fan and W. Yang, *J. Alloys Compd.*, , DOI:10.1016/j.jallcom.2020.154118.

30 T. Deng, W. Zhang, O. Arcelus, D. Wang, X. Shi, X. Zhang, J. Carrasco, T. Rojo and W. Zheng, *Commun. Chem.*, 2018, 1.

31 31 S. Sun, D. Rao, T. Zhai, Q. Liu, H. Huang, B. Liu, H. Zhang, L. Xue and H. Xia, *Adv. Mater.*, 2020, **32**, 1–11.

32 D. Prakash and S. Manivannan, *J. Alloys Compd.*, 2021, **854**, 156853.

33 C. Wang, Z. Song, H. Wan, X. Chen, Q. Tan, Y. Gan, P. Liang, J. Zhang, H. Wang, Y. Wang, X. Peng, P. A. van Aken and H. Wang, *Chem. Eng. J.*, 2020, **400**, 125955.

34 R. Wang, H. Xuan, G. Zhang, H. Li, Y. Guan, X. Liang, S. Zhang, Z. Wu, P. Han and Y. Wu, *Appl. Surf. Sci.*, 2020, **526**, 146641.

35 Z. Andikaey, A. A. Ensafi and B. Rezaei, *Int. J. Hydrogen Energy*, 2020, **45**, 32059–32071.